Developing an Economical Wear and Corrosion Resistant Fe-Based Metallic Glass Composite Coating by Plasma and HVOF Spraying

Sapan K. Nayak[1] · Anil Kumar[1] · Tapas Laha[1]

Abstract Recently, thermal spraying processes are receiving great attention from the research community for the development of Fe-based metallic glass (MG) composite coatings possessing unique combination of improved mechanical and corrosion properties. At the same time, selection of thermal spraying process and deposition parameters are critical, as coating characteristics including porosity and amorphicity are highly dependent on these factors, and such characteristics have significant influence on both mechanical and corrosion properties. Accordingly, in this work, two prominently used thermal spraying methods; atmospheric plasma spraying (APS) and high-velocity oxy-fuel (HVOF) spraying were employed to synthesize an economical in-situ MG composite coating system based on a newly developed FeCrBPC alloy ($Fe_{63}Cr_9P_5B_{16}C_7$). This was done to establish a comprehensive correlation between process-microstructure-wear and corrosion resistance for Fe-based MG composite coating prepared via different thermal spraying processes. Microstructural characterization revealed lower amount of porosity and reduced amorphicity for HVOF-coating compared to APS counterpart. The HVOF-coating exhibited higher wear and corrosion resistance, attributed to the better combination of porosity content and level of amorphicity. Most importantly, both the composite coatings exhibited superior wear and corrosion resistance compared to HVOF-sprayed SS316L coating prepared using industrially optimized parameters.

Keywords atmospheric plasma spraying (APS) · corrosion · Fe-based metallic glass composite coating · high velocity oxy-fuel (HVOF) spraying · wear

✉ Sapan K. Nayak
   sapan.nayak94@gmail.com

✉ Tapas Laha
   laha@metal.iitkgp.ac.in

1 Department of Metallurgical and Materials Engineering, Indian Institute of Technology, Kharagpur 721302, India

Introduction

Because of excellent combination of mechanical and corrosion properties of metallic glass (MG) systems, inexpensive Fe-based MG coatings with various compositions have gained significant attention to provide surface protection for structural components in aggressive environments (Ref 1-4). Regrettably, lack of plasticity at room temperature is the major bottleneck of such monolithic MG coatings, which limits their practical engineering applications (Ref 5, 6). Thus, developing an in-situ composite structure viz. glassy matrix embedded with secondary crystalline phases is considered very useful to circumvent the inherent brittleness of these coatings (Ref 6-8). The above-mentioned scenarios led to an enhanced drive for the research on exploring various Fe-based MG composite coatings (Ref 9-13).

Over the past decade or so, various thermal spraying methods are being employed in preparing such composite

coatings because of the higher rate of deposition, lower cost of operation and ability to coat the substrates with complex geometry (Ref 1, 6, 14). Previous studies have demonstrated that mechanical and tribological properties of Fe-based MG coatings could be strengthened via dispersion of crystalline phases (Ref 15-17). This was because of impeded shear band propagation and nucleation of additional shear bands prompted by crystalline phases present in the glassy matrix along with increased hardness and improved plasticity. At the same time, the presence and/or evolution of such crystalline phases can have deleterious influence on corrosion properties of MG coatings (Ref 18-21). In addition, entrapment of porosities is unavoidable in the thermal sprayed coatings, and the wear, as well as the corrosion properties, are substantially affected by the entrapped porosity resulting in hastened deterioration of the coating (Ref 16, 22, 23). It is possible to obtain a coating with well-balanced level of amorphicity and porosity by optimizing the process parameters of thermal spraying (Ref 24-26). However, prior to even optimizing these parameters for synthesizing superior quality coating, the initial decision is about the selection of the spraying technique.

The primary characteristics of the thermal sprayed MG coatings, including degree of amorphicity, microstructural evolution and porosity content are significantly influenced by attributes of different thermal spraying processes (majorly defined by the attributes of in-flight particles, viz. temperature and velocity). Among all the spraying techniques, atmospheric plasma spraying (APS) and high-velocity oxy-fuel (HVOF) methods were reported to be efficient in producing Fe-based MG coatings, which are characterized by higher thermal and higher kinetic energies of the in-flight powder particles, respectively, consequently affecting microstructural as well as compositional evolution in the coatings. Thus, in this context, selection of thermal spraying method is crucial to synthesize MG coatings with desired properties. In the past, the comparative study between Fe-based MG composite coating developed by APS and HVOF processes has rarely been discussed in the existing literature.

Apart from all the factors discussed above, chemical composition is the most important factor in determining wear and corrosion properties of Fe-based MG alloys (Ref 27, 28). Although wear and corrosion properties of various thermal sprayed Fe-based MG coatings have already been investigated, the studied alloy systems primarily contained higher amounts of Cr and Mo, along with occasional addition of Ni, Cu, Nb, Y, W, etc. However, these elements are expensive which limits the widespread applications of these alloys. The addition of inexpensive metalloids (e.g., C, P and B) significantly improves the glass-forming ability of Fe-based systems (Ref 27, 28). Therefore, synthesizing a

Fe-Cr-based MG alloy with low-cost metalloids without addition of expensive elements is of great significance for wear and corrosion-resistant applications.

Accordingly, a low Cr and inexpensive metalloid containing Fe-based ($Fe_{63}Cr_9P_5B_{16}C_7$, at.%) composite coating was developed by two different thermal spraying processes (APS and HVOF) in this work with previously optimized deposition parameters based on authors' earlier works (Ref 29, 30), to investigate the potential for its use as an economical surface protective coating. A systematic investigation was carried out to understand the influence of in-flight particle characteristics (viz. temperature and velocity) of thermal spraying processes on microstructure as well as phase evolution of the coatings, and their subsequent influence on wear and corrosion properties. Multiscale wear tests (nanoscratch and dry sliding wear) were carried out to examine the effect of porosity as well as constituent phases in the coatings; while potentiodynamic polarization and electrochemical impedance spectroscopy along with post-corroded sample characterization (morphology and composition) were conducted to understand the corrosion behavior. The properties of MG composite coatings were also compared with HVOF-sprayed stainless steel (SS316L) coating and mild steel substrate to estimate the relative protection ability.

Experimental Procedure

Fe-based feedstock powder of composition $Fe_{63}Cr_9P_5B_{16}C_7$, at.% was prepared by water atomization process using industrial grade raw materials. The water atomization was carried out with atomization pressure of 160 bar, metal flow rate of 25 to 30 kg min^{-1}, water flow rate of 280 L·min^{-1} while maintaining inert (Ar) atmosphere in the atomization chamber. This feedstock powder was deposited on grit-blasted mild steel plates via two different thermal spraying processes; APS (Plasma F-4, MEC, India) and HVOF (HIPOJET-2700, MEC, India) to synthesize the coatings. For convenience, coatings prepared by APS and HVOF processes are designated as APS-coating and HVOF-coating, respectively. All the spraying parameters were optimized based on authors' previous works (Ref 29, 30), and the parameters are shown in Table 1. For comparison, stainless steel coating (SS316L) was also prepared by HVOF technique with industrially optimized parameters, represented as SS-coating. The reason behind selection of HVOF method for deposition of SS-coating was to obtain a denser coating possessing superior hardness and corrosion properties compared to the APS-sprayed counterpart (Ref 31).

Microstructural details of the powder and the coatings were analyzed with a scanning electron microscope (SEM,

Table 1 Process parameters used for synthesizing Fe-based metallic glass composite coatings by APS- and HVOF-spraying

APS spraying

Process parameters	Primary gas (Ar) flow rate, L/min	Secondary gas (H_2) flow rate, L/min	Plasma power, kW	Spray distance, mm	Powder feed rate, g/min
	60	10	30	120	40

HVOF spraying

Process parameters	Oxygen flow rate, L/min	Fuel gas flow rate, L/min	Air flow rate, L/min	Carrier gas flow rate, L/min	Spray distance, mm	Powder feed rate, g/min
	270	55-60	460	15-18	150	50

SUPRA 40, Carl Zeiss AG, Germany). Porosity content (vol.%) in the coatings was measured by area analysis method with ImageJ k 1.45 software from ten polished cross-sectional SEM micrographs (captured at 500X). Phase composition of the powder as well as the coatings was examined via x-ray diffraction (XRD, DY1705, Empyrean, PANalytical, Netherlands) using Cr-Kα radiation. Evolution of various phases in the coatings was further investigated using a transmission electron microscope (FEG-TEM, JEOL, JEM-2100F).

Microhardness value was estimated based on 15 measurements performed at a load of 25 gf using a Vickers micro indenter (UHLVMHT-001, Walter Uhl, Germany). Nanoindentation and nanoscratch experiments were carried out by a Triboindenter (TI 950, Hysitron Inc., USA) using Berkovich tip (TI-0039, Hysitron Inc., USA). The testing parameters for nanoindentation were; maximum load of 5000 μN, loading rate of 500 μN/s and peak load hold time of 10 s, and the average value of nanohardness was acquired based on 100 indents (10 × 10 matrix of indents). Constant low load nanoscratch tests (load of 5000 μN) were carried out with a traverse speed of 0.5 μm/s to obtain a scratch length of 10 μm. Scratch trails were recorded with an in-situ scanning probe microscope (SPM) to investigate the morphology and evaluate nano-wear volume of the tracks. Dry sliding wear test was performed by a pin-on-disc tribometer (TE97 Friction and Wear Demonstrator, Phoenix Tribology Ltd., England) using sample as pin and rotating Al_2O_3 disc. The parameters used were; applied load of 10 N, rotating speed of 0.26 m/s and a sliding distance of 235 m. At least three sliding tests were conducted for each sample from the repeatability perspective.

Corrosion behavior of the samples was evaluated by conducting potentiodynamic polarization and electrochemical impedance spectroscopy (EIS) tests in 3.5 wt.% NaCl environment, with a potentiostat (Interface 1000, Gamry Instruments, USA). A conventional three-electrode cell having graphite counter electrode, saturated calomel reference electrode (SCE) and coating/substrate working electrode was used for corrosion experiment. The polarization test was performed with a scan rate of 0.5 mV/s post immersion in the electrolyte for 1 h, for stabilization of open circuit potential (OCP). EIS study was carried out using 10 mV sinusoidal amplitude in 10^5 to 10^{-2} Hz frequency range at OCP. Acquired EIS spectra were analyzed and fitted using Gamry EChem Analyst software. From good reproducibility point of view, the tests were repeated three times for each sample. Surface of the corroded samples was inspected by SEM to observe the morphology of the post-corroded samples. Besides, compositional analysis of corrosion products was carried out by Raman spectroscopy (InVia Raman Microscope, Renishaw, UK) using Co laser of 532 nm wavelength.

Results and Discussion

Characterization of Feedstock Powder

Morphology along with phase constitutions of the feedstock powder is presented in Fig. 1. Nearly spherical morphology of the powder (Fig. 1a) is associated with the optimized parameters of water atomization. It was observed from Fig. 1(a), that powder size varied within 5 to 50 μm with mean size of 18 μm. Powders with this particular size along with nearly spherical morphology favor improved flowability during thermal spraying (Ref 16, 24). Fig. 1(b) illustrated the XRD result for the powder displaying a broad hump superimposed with several crystalline peaks, implying glassy structure of the powder having some amount of crystalline phases. Genesis of glassy structure in the powder was because of the high glass-forming ability of this particular composition (P_{HSS} = -7.31 kJ/mol) as well as sufficiently higher cooling rate of water atomization process. P_{HSS} is a thermodynamic parameter used for the prediction of glass-forming ability
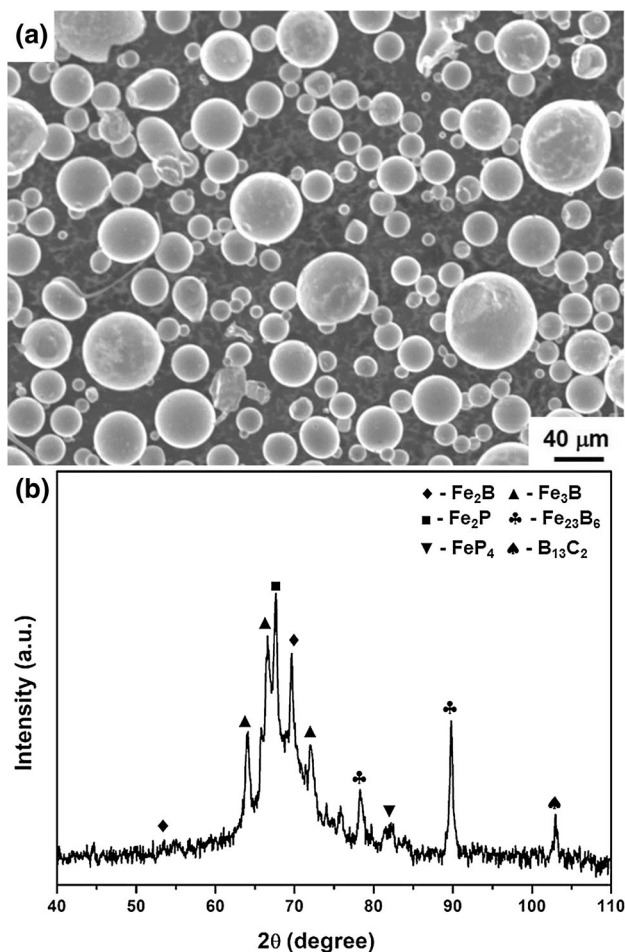
Fig. 1 (a) SEM micrograph and (b) XRD pattern of Fe-based feedstock powder ($Fe_{63}Cr_9B_{16}C_7P_5$, at.%) used for depositing the different metallic glass composite coatings

in multi-component systems, and it can be calculated by using an equation as given below (Ref 32):

$$P_{HSS} = \Delta H_{mix}(\Delta S_{mix}/R)(\Delta S_\sigma/k_B) \qquad (Eq\ 1)$$

where ΔH_{mix} is enthalpy of mixing, ΔS_{mix} is configurational entropy, R is gas constant, ΔS_σ is mismatch entropy and k_B is Boltzmann's constant. P_{HSS} value of the present Fe-based alloy composition has been calculated and reported elsewhere by the authors (Ref 30). The estimated value of P_{HSS} parameter (− 7.31 kJ/mol) lies well within the required range (−11 kJ/mol to −3 kJ/mol) of glass formation which has been established by previously reported experimental results supported with computational analysis (Ref 32, 33).

Microstructural- and Compositional-Analysis of the Coatings

Morphological details of as-sprayed surface of the coatings prepared with APS- and HVOF-spraying are shown in

Fig. 2(a) and (b), whereas the polished microstructural details of the coatings (both top surface and cross-sectional morphology) are presented in Fig. 2(c) and (d). The surface of APS-coating exhibited considerably higher degree of melting of the powders (Fig. 2a) compared to HVOF-coating (Fig. 2b), attributed to the higher heat input associated with plasma spraying process. However, the polished top, as well as cross-sectional surfaces of APS-coating (Fig. 2c), showed higher amount porosity content compared to HVOF-coating (Fig. 2d). Moreover, the cross-sectional micrographs (insets of Fig. 2c and d) exhibited better inter-splat bonding for HVOF-coating, ascribed to the higher velocity along with heavier impact of in-flight powder particles in HVOF spraying process. The thickness for APS- and HVOF-sprayed coatings was measured as 162 ± 15 and 167 ± 13 μm, respectively, while the cross-sectional porosity content was found to be approximately 3.4 ± 0.8 and 1.3 ± 0.3 (vol.%), respectively. To mention, the amount of porosity for HVOF-sprayed SS-coating was around 1.2 ± 0.3 (vol.%). These results envisaged that the morphology and the microstructural characteristics (amount and size of porosity, inter-splat bonding, etc.) for the coatings are significantly influenced by the in-flight particles characteristics (temperature and velocity) of different thermal spraying processes.

Evolution of various phases in the coatings was examined by XRD analysis as shown in Fig. 3, which showed broad humps overlapped with some crystalline peaks, indicating glassy/crystalline composite structure for both the coatings. The crystalline peaks were matched with α-Fe, Fe_2B, $Fe_{23}B_6$, Fe_3B, FeB and FeP_4 phases. Amorphicity level of APS- and HVOF-sprayed coatings evaluated based on the area ratio of crystalline peaks to glassy halo peak was approximately 85.2 and 74.6%, respectively (Ref 34). Formation of crystalline phases can be ascribed to the heat input, the heat build-up, the presence of pre-existing crystalline phases and the surface oxidation of molten/semi-molten particles during thermal spraying (Ref 16, 18, 25, 35, 36). The higher level of amorphicity for APS-coating compared to HVOF-coating can be attributed to higher degree of amorphization because of accelerated cooling rate resulting from higher amount of superheat in molten in-flight particles during plasma spraying process.

Further, TEM micrographs and HRTEM images as shown in Fig. 4 revealed the presence of nano-sized crystalline phases in glassy matrix of both the coatings, but the volume fraction of crystalline phases was higher for HVOF-coating. Moreover, SAD patterns (insets of Fig. 4a and b) exhibited an increased number of spots in diffused rings from APS-coating to HVOF-coating, which validated the higher amorphicity for the plasma sprayed coating. The results of TEM study are consistent with XRD results (Fig. 3) discussed above, which clearly demonstrated that

Fig. 2 SEM micrographs of (a, b) as-sprayed surface and (c, d) polished top surface and cross-sectional morphology (in insets) of APS- and HVOF-sprayed coatings, illustrating the difference in degree of melting and porosity distribution
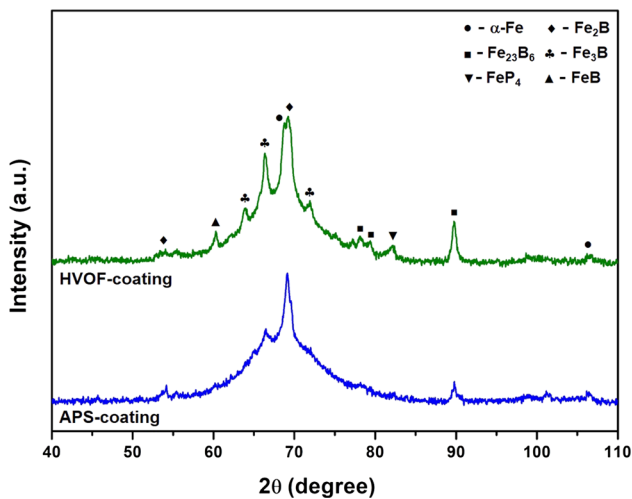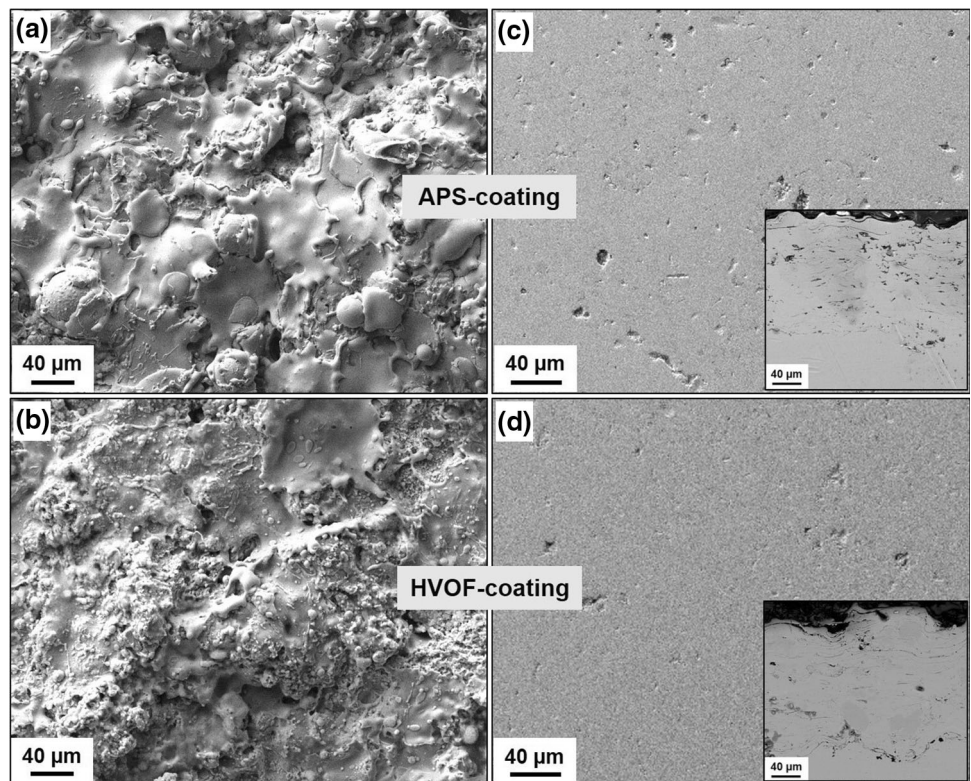

Fig. 3 XRD patterns of APS- and HVOF-sprayed coatings, displaying the variation in extent of crystallization

extent of amorphization, as well as phase evolution, are highly dependent on the heat input level of different thermal spraying process.

Mechanical Properties of the Coatings

Different mechanical properties of the samples obtained from micro- and nano-indentation tests are reported in Table 2. Average Vickers microhardness ($HV_{0.025}$) of mild steel, SS-coating, APS-coating and HVOF-coating was 173 $\pm$ 9, 712 $\pm$ 41, 1032 $\pm$ 78 and 1127 $\pm$ 52, respectively, and average nanohardness (H) were approximately 3.6 $\pm$ 0.2, 7.3 $\pm$ 1.9, 10.5 $\pm$ 2.5 and 11.4 $\pm$ 2.1, respectively. The ultra-high hardness values for APS- and HVOF-sprayed coatings compared to SS-coating as well as mild steel was because of the presence of composite structure (glassy matrix embedded with nanocrystalline phases) in the coatings. Furthermore, it should be pointed out that despite the similarity in amount of porosity for both the coatings, the hardness of HVOF-coating was found to be higher than that of APS-coating. This indicated the higher value of hardness for HVOF-coating has actually resulted from a synergistic effect of better inter-splat bonding (Fig. 2) and presence of higher amount of harder intermetallic phases in the glassy matrix of the coating (evident from Fig. 3).

Multi-scale Wear Properties of the Coatings

Nano-scale Wear

Because of the presence of various heterogeneities in thermal sprayed coatings, including multi-layered splats, porosities, etc.; deformation behavior of individual splats can only be studied by lower length scale test using lower level of loading (Ref 37). While, the effect of overall coating characteristics on the wear properties can be investigated with higher length scale tests like macro-wear,

Fig. 4 (a, b) TEM micrographs with corresponding SAED patterns in insets and (c, d) HRTEM micrographs of APS- and HVOF-sprayed coatings, revealing the variation in amorphicity
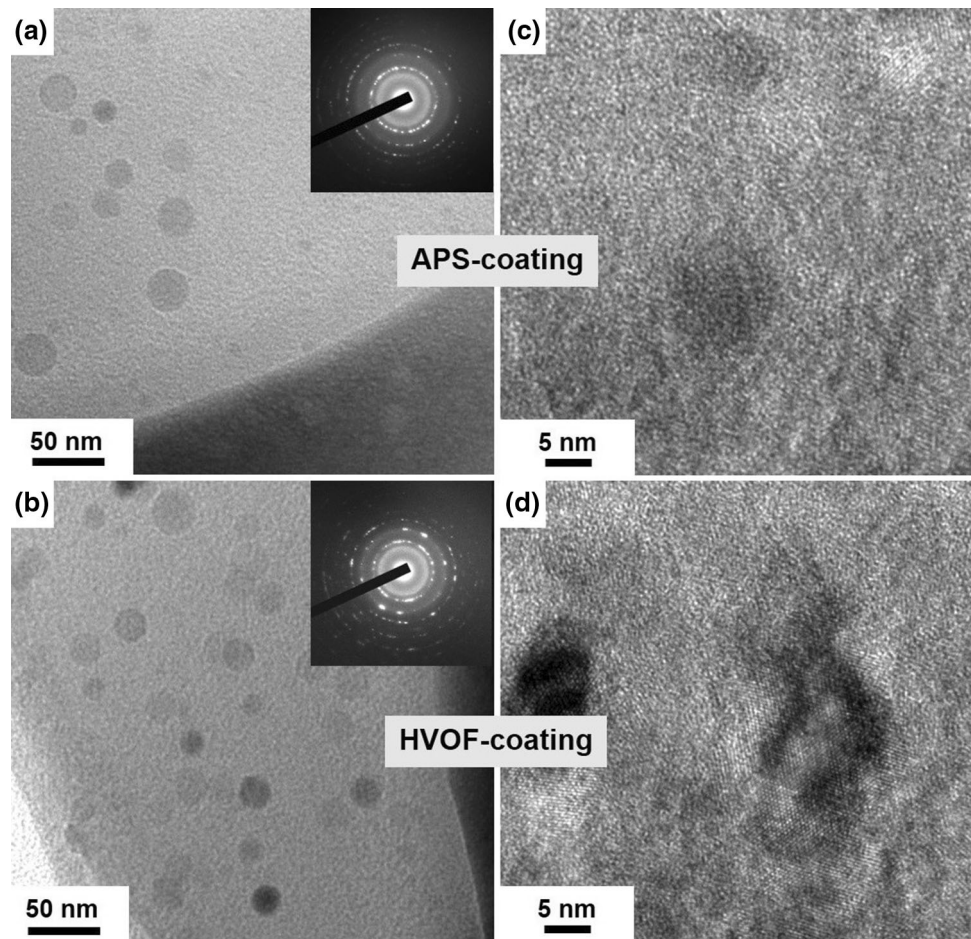

Table 2 Mechanical properties acquired from microindentaion, nanoindentaion and multi-scale wear tests of the different coatings and the substrate

Sample	Mild steel (substrate)	SS316L coating	Metallic glass composite coating	
		SS-coating (HVOF)	APS-coating	HVOF-coating
Nanohardness, H, GPa	3.6 ± 0.2	7.3 ± 1.9	10.5 ± 2.5	11.4 ± 2.1
Vickers micro-hardness, $HV_{0.025}$	173 ± 9	712 ± 41	1032 ± 78	1127 ± 52
Nano-scratch depth, nm	…	118.4 ± 1.1	61.5 ± 1.2	37.9 ± 0.8
Nano-wear volume per unit length, $\times 10^3$ nm^3/nm	…	2.36 ± 0.03	0.64 ± 0.05	0.24 ± 0.02
Coefficient of friction (dry sliding wear)	0.53 ± 0.06	0.28 ± 0.02	0.18 ± 0.03	0.14 ± 0.02

which has been discussed later in this section. Thus, low load nanoscratch experiment was conducted for understanding the influence of phase composition on single splat wear behavior of the various coatings. In this method, wear resistance of the coatings was estimated from scratch groove characteristics (viz. depth and width of scratch) and wear volume. SPM images of scratch trails along with corresponding cross-sectional depth profiles are presented in Fig. 5. The SPM images (Fig. 5a–c) exhibited significant differences in the scratch width and depth of the various

coatings, indicating different responses against wear of these coatings. When standard Berkovich tip is utilized for nanoscratch test, then wear volume (W_V) per unit length of the scratch, which is directly related to the wear rate, can be calculated by using Eq. 2 (Ref 38),

$$W_v = \frac{1}{2}\cos(70.3°) \cdot d_n^2 \quad \text{(Eq 2)}$$

where d_n is normal displacement. It was noticed from the nanoscratch results shown in Table 2, both the MG
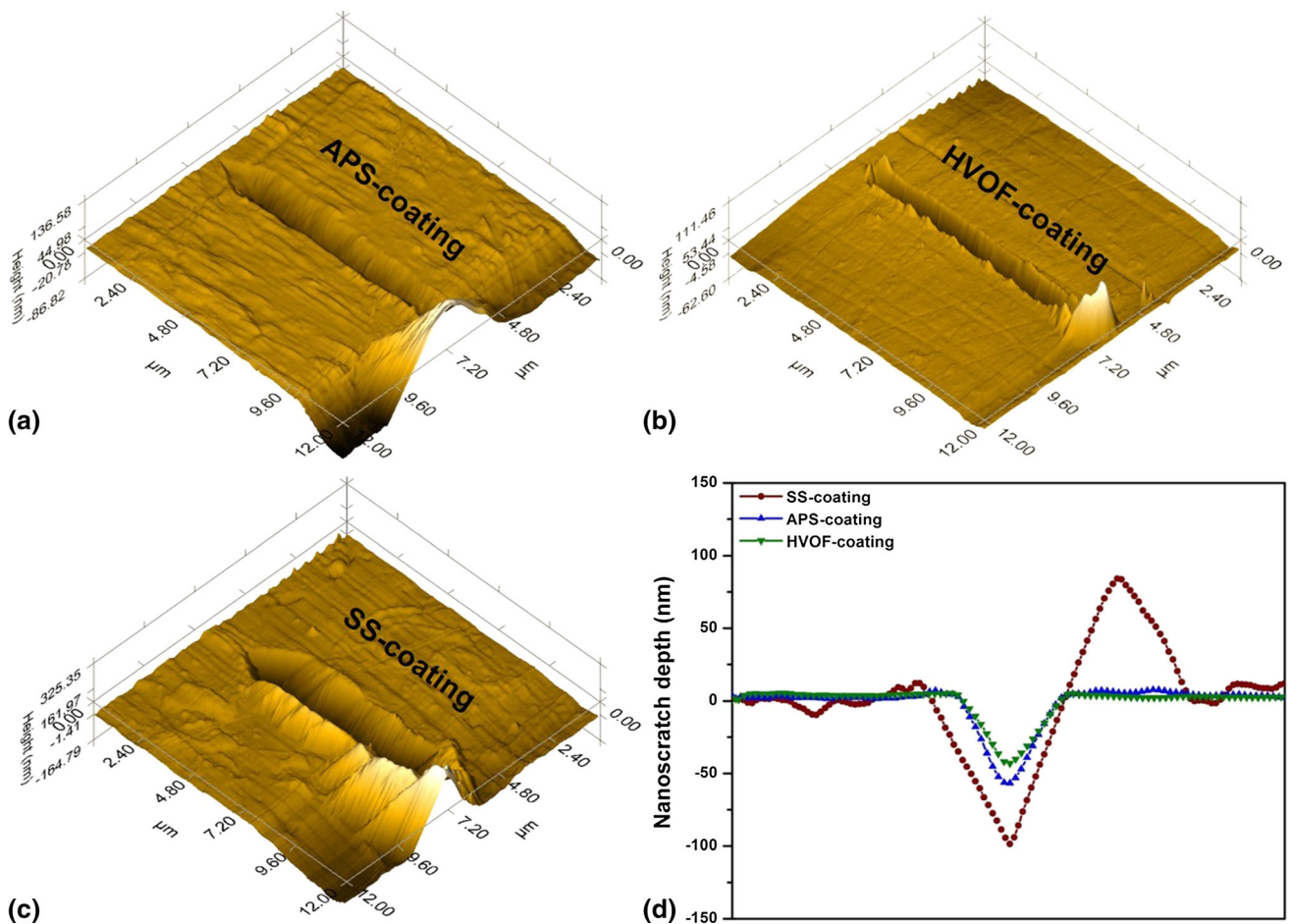
Fig. 5 SPM images of nanoscratch tracks; (a) APS-coating, (b) HVOF-coating and (c) SS-coating, and (d) 2D cross-sectional scratch depth profiles of these coatings

composite coatings displayed lower scratch depth and wear volume than that of SS-coating, establishing their superior wear resistance. Moreover, lower value of wear volume for HVOF-coating compared to APS-coating can be attributed to existence of higher content of harder intermetallics in the glassy matrix.

Macro-scale Wear

The over-all deformation behavior of the various coatings can be estimated with the help of macro-wear characterization (dry sliding wear test), as the interaction volume during such test incorporates every heterogeneities of the coatings (inter-splats, pores, crystalline phases, etc.). The results obtained from the dry sliding wear study are presented in Fig. 6. Specific wear rate (W in mm³/Nm) can be calculated by using Eq. 3 (Ref 8),

$$W = \frac{V}{S \cdot F} \qquad \text{(Eq 3)}$$

where V is wear volume, S is sliding distance and F is applied load, and the obtained wear rate values are presented in Fig. 6(a). It can be noticed that, both the MG composite coatings displayed significantly reduced wear rate compared to SS-coating and mild steel, because of higher hardness of the MG coatings. In addition, the lower wear rate of HVOF-coating compared to APS-coating can be ascribed to the denser microstructure (lower porosity and better inter-splat bonding) along with presence of relatively higher content of hard intermetallics. The coefficient of friction (COF) curves as a function of sliding distance are demonstrated in Fig. 6(b), and the average values of COF are presented in Table 2. The values of COF further confirmed the better anti-wear properties of MG composite coatings compared to SS-coating and the substrate. Moreover, the lowest value of COF observed in case of HVOF-coating implied its best anti-wear properties among all the samples.
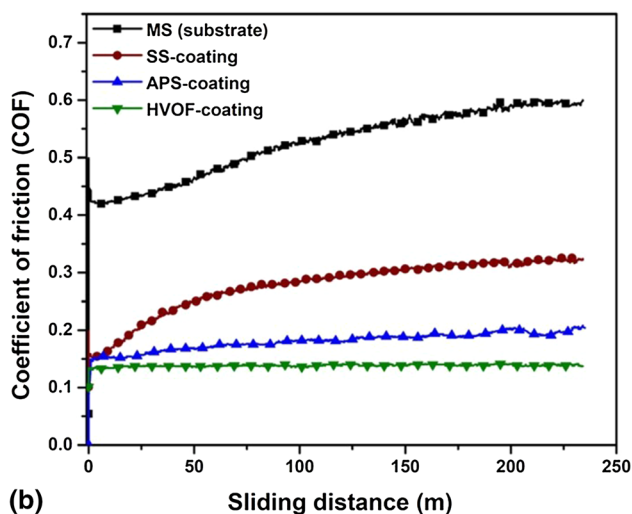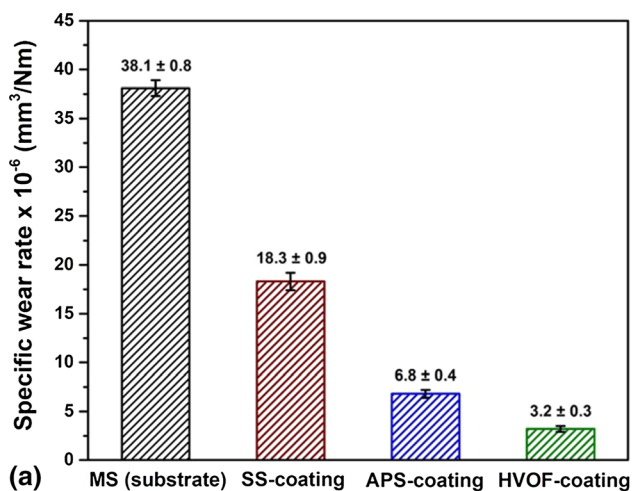
Fig. 7 Potentiodynamic polarization curves of the various coatings and mild steel in 3.5 wt.% NaCl solution

Fig. 6 (a) Bar graph of wear rate (b) coefficient of friction versus sliding distance curves of the different coatings and mild steel obtained from dry sliding wear study

Corrosion Properties of the Coatings

Potentiodynamic Polarization and Electrochemical Impedance Spectroscopy Studies

The corrosion behavior of the samples was analyzed by potentiodynamic polarization and electrochemical impedance spectroscopy, and the corresponding results are depicted in Figs. 7 and 8, respectively. Values of different corrosion properties extracted from polarization curves (Fig. 7) are reported in Table 3. It was noticed that SS-coating exhibited spontaneous passivation behavior (though a weak one) as opposed to delayed passivation of both the MG composite coatings. On the other hand, the mild steel experienced active corrosion throughout the anodic polarization scan. The delayed or pseudo-passivation for partially crystallized Fe-based MG alloy was noticed in the past by Ha et al. (Ref 39). Moreover, same

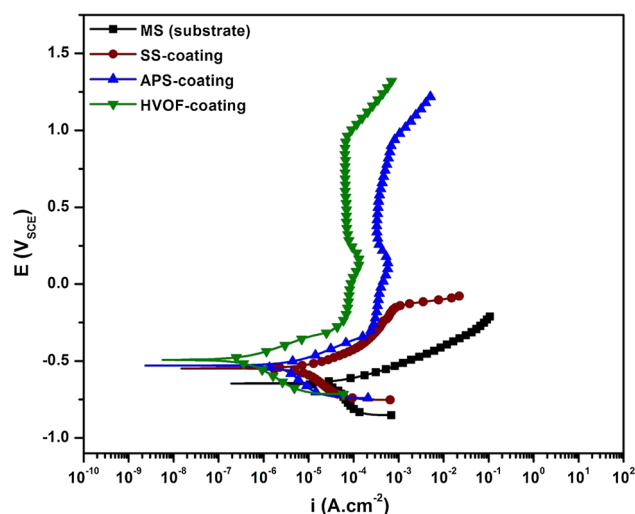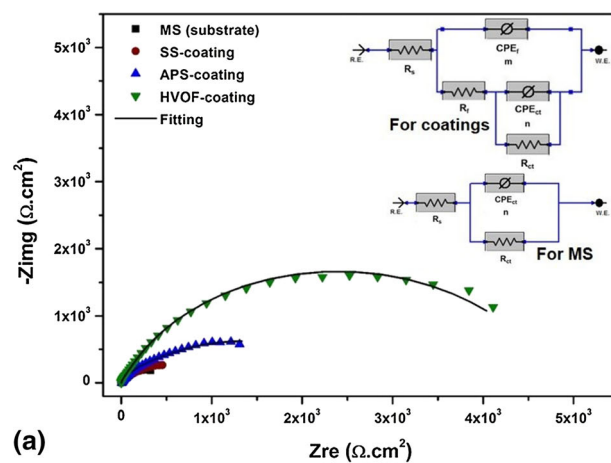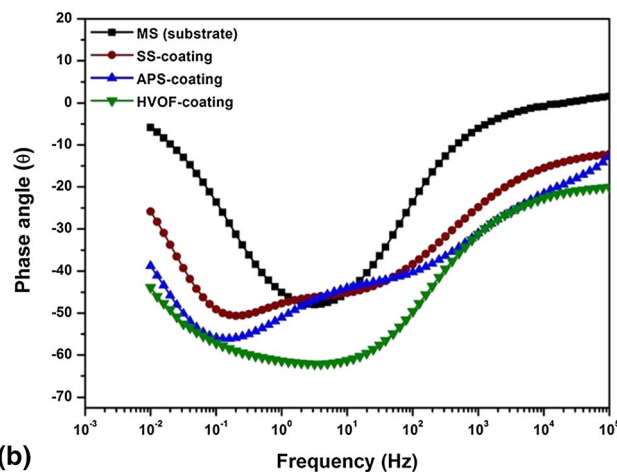**Fig. 8** EIS plots of the different coatings and mild steel in 3.5 wt.% NaCl solution at OCP; (a) Nyquist plot (inset: electrical equivalent circuits used for EIS data fitting) and (b) Bode phase angle plot

kind of potentiodynamic polarization plot for APS- and

Table 3 Corrosion properties obtained from potentiodynamic polarization and electrochemical impedance spectroscopy studies of the various coatings and the substrate in 3.5 wt.% NaCl solution

Sample	Mild steel (substrate)	SS316L coating	Metallic glass composite coating	
		SS-coating (HVOF)	APS-coating	HVOF-coating
Potentiodynamic polarization				
E_{corr}, mV_{SCE}	$- 647 \pm 12$	$- 549 \pm 5$	$- 541 \pm 8$	$- 507 \pm 6$
i_{corr}, $\mu A\ cm^{-2}$	39.2 ± 2.7	11.8 ± 0.5	7.5 ± 0.8	1.4 ± 0.4
i_{pass}, $\mu A\ cm^{-2}$	…	253.1 ± 7.3	340.4 ± 12.7	68.5 ± 5.4
		@ $- 300\ mV_{SCE}$	@ $500\ mV_{SCE}$	@ $500\ mV_{SCE}$
E_{pit}, mV_{SCE}	…	$- 147 \pm 6$	894 ± 11	942 ± 5
Electrochemical impedance spectroscopy				
R_s, $k\Omega\ cm^2$	0.005 ± 0.002	0.003 ± 0.001	0.009 ± 0.002	0.008 ± 0.002
Q_f, $\mu S\ s^m\ cm^{-2}$	…	2960 ± 47	1276 ± 35	247 ± 9
m	…	0.69 ± 0.02	0.71 ± 0.02	0.77 ± 0.01
R_f, $k\Omega\ cm^2$	…	0.43 ± 0.04	0.82 ± 0.07	1.46 ± 0.08
R_{ct}, $k\Omega\ cm^2$	0.68 ± 0.06	0.96 ± 0.09	1.63 ± 0.11	3.73 ± 0.19
Q_{ct}, $\mu S\ s^n\ cm^{-2}$	1540 ± 46	1073 ± 37	742 ± 32	357 ± 14
n	0.61 ± 0.03	0.63 ± 0.02	0.65 ± 0.02	0.72 ± 0.02
$R_t = R_f + R_{ct}$, $k\Omega\ cm^2$	0.68 ± 0.06	1.39 ± 0.13	2.45 ± 0.18	5.19 ± 0.27
Goodness of fit, $\times 10^{-4}$	7.3 ± 1.1	3.2 ± 0.9	4.6 ± 0.7	5.8 ± 0.6

HVOF-sprayed coatings of the present work, has also been noted earlier by Wang et al. in Fe-based MG coating (Ref 40).

Among all the samples, HVOF-coating displayed superior corrosion resistance in terms of noblest E_{corr}, lowest i_{corr}, highest E_{pit} and lowest i_{pass} values, despite of having reduced level of amorphicity than that of APS-coating. This enhanced corrosion resistance for HVOF-coating can be ascribed to (i) denser microstructure (viz. decreased porosity) and (ii) lower degree of crystallization than a certain critical value. Gan et al. (Ref 41) observed that corrosion properties of Fe-based MG system remained almost unaffected below the critical value of crystallinity (30% in that study); while a remarkable decrease in corrosion resistance was noted above the critical value. It was pointed out that, when the crystallization volume fraction was lower than the critical value, the corrosion process was controlled by passivation along with metastable pitting possessing the potential for re-passivation; while the corrosion mechanism was governed by micro galvanic effect-strengthened stable pitting above critical value of crystallinity. Additionally, the exact value of such a critical fraction of crystallization in the present Fe-based MG alloy composition still needs to be established, which the authors intend to address during their continued work on thermal sprayed Fe-based MG coatings.

The significant difference between i_{corr} and i_{pass} values of both APS- and HVOF-sprayed coatings suggested their increased sensitiveness for localized corrosion (Ref 42). Moreover, the higher susceptibility for localized corrosion in case of SS-coating (despite of lower porosity), as indicated by limited passive region and lower value of E_{pit}, was the reason behind its poor corrosion resistance compared to both the MG composite coatings. The degraded corrosion properties of SS-coating can be ascribed to the existence of chemical heterogeneities as well as crystalline defects, which led to weakened stability of passive film on SS-coating.

The results of EIS analysis are presented as Nyquist (Fig. 8a) along with Bode phase angle (Fig. 8b) plots. The corrosion resistance can be estimated from the size of semicircles in Nyquist plot (Ref 43); and it followed an increasing trend, mild steel < SS-coating < APS-coating < HVOF-coating, establishing the highest corrosion resistance for HVOF-coating. Apart from this, the two phase angle maxima observed in Bode plot for the coatings suggested the existence of two time constants; one at high frequency is for surface film, while the other one corresponds to charge transfer resistance (Ref 44). Values of phase angle maximum for mild steel, SS-coating, APS-coating and HVOF-coating were 47°, 51°, 56° and 64°, respectively, and the highest phase angle maxima for HVOF-coating indicated its improved corrosion resistance. Moreover, HVOF-coating displayed a wider phase angle maxima, implying the improved chemical stability.

Based on the above-mentioned concepts, two different electrical equivalent circuits (inset in Fig. 8a) were used for EIS data fitting, and the fitted data are presented in Table 3. These equivalent circuits contained the following elements; solution resistance (R_s), film resistance (R_f), charge transfer resistance (R_{ct}), film capacitance (Q_f) and double-layer capacitance (Q_{ct}) (Ref 21, 45, 46). Constant phase element

Fig. 9 Post-corroded surface morphology of (a) APS-coating (b) HVOF-coating and (c) SS-coating, revealing the extent of corrosion after potentiodynamic polarization test
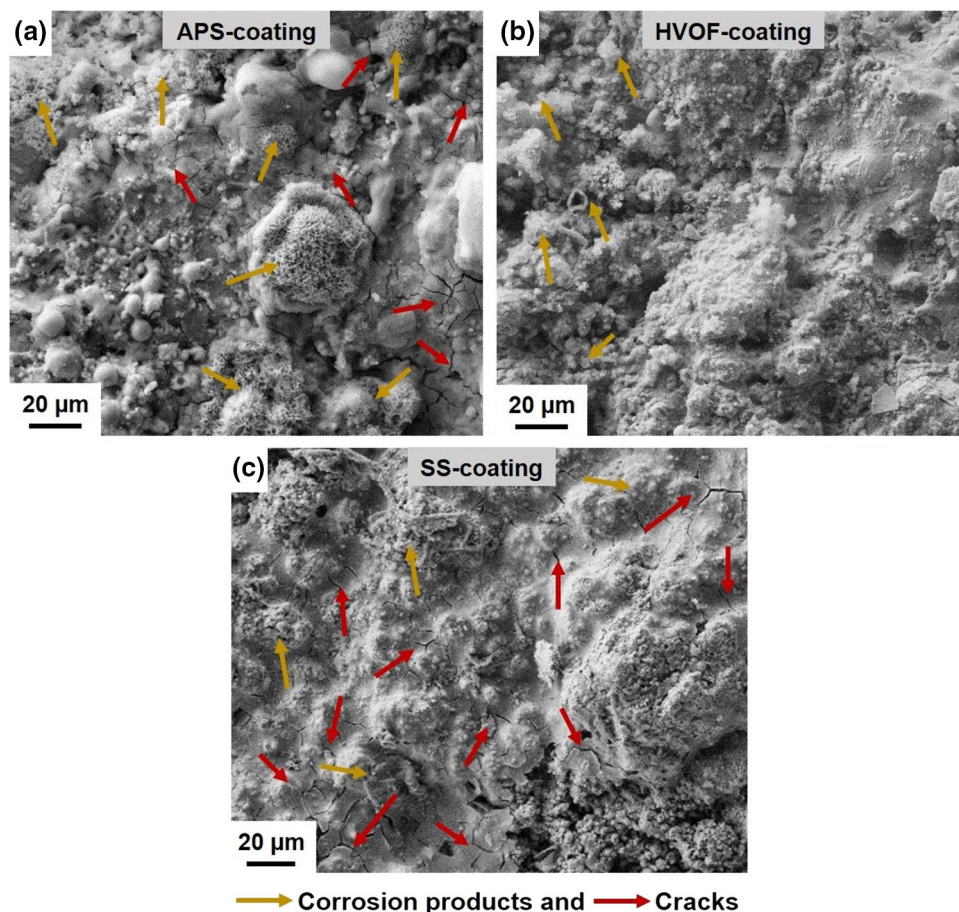
was utilized rather than pure capacitor in the circuit, ascribed to the surface heterogeneity of the samples. The corrosion resistance can be estimated based on the total resistance, R_t (summation of R_f and R_{ct}), since R_t is nearly similar to polarization resistance. The value of R_t (reported in Table 3) was found as 0.68 ± 0.06, 1.39 ± 0.13, 2.45 ± 0.17 and 5.19 ± 0.28 kΩ cm^2 for mild steel, SS-coating, APS-coating and HVOF-coating, respectively, further confirming the superior corrosion resistance of HVOF-coating. These outcomes of EIS study are consistent with inference of polarization results discussed above.

The current results provide an important implication that a thermal sprayed Fe-based MG composite coating with desired corrosion properties can be developed by minimizing the deleterious effect of crystallization through controlled level of crystallinity in the coatings.

Characterization of Post-corroded Samples

For understanding the corrosion process, it is necessary to investigate the post-corroded samples with respect to morphological and compositional changes on the surfaces, and the results of such analyses will be discussed in this section.

Morphology of the Corroded Surface Post-corroded surfaces of the coatings were examined to understand the extent of corrosion degradation as well as localized corrosive attack on the samples, and SEM images of the corroded surface of different coatings are presented in Fig. 9. For APS-coating (Fig. 9a), larger portion of the coating's surface was non-uniformly covered with corrosion products (marked with orange arrows) along with several cracks (red arrows). However, almost no cracks and only presence of corrosion products were observed for HVOF-coating (Fig. 9b), elucidating the enhanced corrosion resistance. Besides, the presence of higher amount of cracks on the surface of SS-coating (Fig. 9c) indicated the poor corrosion resistance. These findings are in line with the results of polarization and EIS studies discussed previously ("Potentiodynamic Polarization and Electrochemical Impedance Spectroscopy Studies" section).

Composition of Corrosion Products Compositional analysis of the corrosion products formed on the surface of the samples was performed by Raman spectroscopy, and the results are depicted in Fig. 10. The acquired spectra revealed the presence of hematite (α-Fe$_2$O$_3$), goethite (α-FeOOH), chromium hydroxide (α-CrOOH), chromium
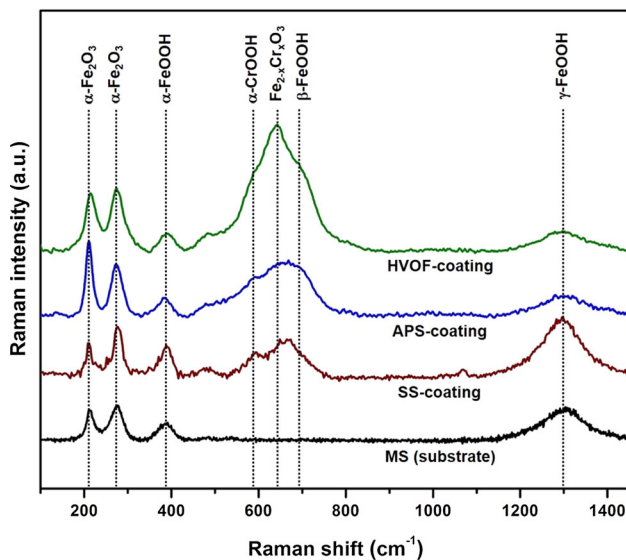
Fig. 10 Raman spectra of the different coatings and mild steel, illustrating the evolution of chromium hydroxide and various iron oxides and hydroxides

substituted hematite ($Fe_{2-x}Cr_xO_3$), akaganeite (β-FeOOH) and lepidocrocite (γ-FeOOH) phases, excluding mild steel (lack of α-CrOOH, $Fe_{2-x}Cr_xO_3$ and β-FeOOH) (Ref 47-49). Among the detected phases, α-CrOOH and $Fe_{2-x}Cr_xO_3$ are considered protective, α-Fe_2O_3 and α-FeOOH have lower protectiveness; while β-FeOOH and γ-FeOOH are soluble. The amount of a particular phase can be estimated from the intensity of different peaks in the Raman spectrum. It was noticed that the relative fraction of protective phases (α-CrOOH and $Fe_{2-x}Cr_xO_3$) followed an increasing trend, mild steel → SS-coating → APS-coating → HVOF-coating, revealing higher amount of protective phases for HVOF-coating. These results further substantiate the superior corrosion properties of HVOF-sprayed MG composite coating compared to all other samples.

Conclusions

Two different thermal spraying processes, atmospheric plasma spraying (APS) and high-velocity oxy-fuel (HVOF) spraying were employed to prepare Fe-based metallic glass (MG) composite coatings. Primary objective of the present work was to establish a comprehensive correlation between process-microstructure-wear as well as corrosion properties of the different thermal sprayed Fe-based MG composite coatings, and the conclusions were summarized as follows:

1. Microstructural and compositional analyses revealed that HVOF-sprayed coating exhibited lower porosity content, improved inter-splat bonding and lower level of amorphicity than that of APS counterpart.

2. The superior mechanical properties (higher nano- and micro-hardness) and wear resistance (lower nano-wear volume, specific wear rate and coefficient of friction) of HVOF-coating compared to APS-coating were ascribed to the denser microstructure and the presence of relatively higher amount of hard intermetallic phases.

3. The enhanced corrosion resistance (nobler E_{corr}, lower i_{corr}, lower i_{pass}, higher E_{pit} and higher R_t values) of HVOF-coating (despite of reduced amorphicity) was attributed to the lower porosity content, lower degree of crystallinity than a certain critical value (above the critical value, corrosion resistance degrades drastically) along with formation of higher amount of protective phases in the corrosion products.

4. Most importantly, both Fe-based MG composite coatings displayed improved wear and corrosion properties than that of the high Cr-containing stainless steel (SS316L) coating, establishing their suitability as low-cost surface protective coating.

References

1. B. Huang, C. Zhang, G. Zhang and H. Liao, Wear and Corrosion Resistant Performance of Thermal-Sprayed Fe-Based Amorphous Coatings: A Review, *Surf. Coat. Technol.*, 2019, **377**, p 124896. https://doi.org/10.1016/j.surfcoat.2019.124896

2. L. Liu and C. Zhang, Fe-Based Amorphous Coatings: Structures and Properties, *Thin Solid Films*, 2014, **561**, p 70-86. https://doi.org/10.1016/j.tsf.2013.08.029

3. H.R. Ma, X.Y. Chen, J.W. Li, C.T. Chang, G. Wang, H. Li, X.M. Wang and R.W. Li, Fe-Based Amorphous Coating with High Corrosion and Wear Resistance, *Surf. Eng.*, 2017, **33**(1), p 56-62.

4. C. Zhang, L. Liu, K.C. Chan, Q. Chen and C.Y. Tang, Wear Behavior of HVOF-Sprayed Fe-Based Amorphous Coatings, *Intermetallics*, 2012, **29**, p 80-85. https://doi.org/10.1016/j.intermet.2012.05.004

5. W. Wang, C. Zhang, Z.W. Zhang, Y.C. Li, M. Yasir, H.T. Wang and L. Liu, Toughening Fe-Based Amorphous Coatings by Reinforcement of Amorphous Carbon, *Sci. Rep.*, 2017, **7**(1), p 1-10.

6. W. Guo, Y. Wu, J. Zhang, S. Hong, G. Li, G. Ying, J. Guo and Y. Qin, Fabrication and Characterization of Thermal-Sprayed Fe-Based Amorphous/Nanocrystalline Composite Coatings: An Overview, *J. Therm. Spray Technol.*, 2014, **23**(7), p 1157-1180.

7. G.Y. Koga, R. Schulz, S. Savoie, A.R.C. Nascimento, Y. Drolet, C. Bolfarini, C.S. Kiminami and W.J. Botta, Microstructure and Wear Behavior of Fe-Based Amorphous HVOF Coatings Produced from Commercial Precursors, *Surf. Coat. Technol.*, 2017, **309**, p 938-944. https://doi.org/10.1016/j.surfcoat.2016.10.057

8. S.K. Nayak, A. Kumar, A. Pathak, A. Banerjee and T. Laha, Multi-scale Mechanical Properties of Fe-Based Amorphous/

Nanocrystalline Composite Coating Synthesized by HVOF Spraying, *J. Alloys Compd.*, 2020, **825**, p 154120. https://doi.org/10.1016/j.jallcom.2020.154120

9. V. Varadaraajan, R.K. Guduru and P.S. Mohanty, Synthesis and Microstructural Evolution of Amorphous/Nanocrystalline Steel Coatings by Different Thermal-Spray Processes, *J. Therm. Spray Technol.*, 2013, **22**(4), p 452-462.

10. D. Zois, A. Lekatou and M. Vardavoulias, Preparation and Characterization of Highly Amorphous HVOF Stainless Steel Coatings, *J. Alloys Compd.*, 2010, **504**(SUPPL. 1), p S283-S287.

11. Z. Zhou, L. Wang, D.Y. He, F.C. Wang and Y.B. Liu, Microstructure and Electrochemical Behavior of Fe-Based Amorphous Metallic Coatings Fabricated by Atmospheric Plasma Spraying, *J. Therm. Spray Technol.*, 2011, **20**(1-2), p 344-350.

12. P.K. Rai, D. Naidu, B. Satapathy, K. Sarkar, A.S. Pathak, P. Bijalwan, M. Dutta, A. Banerjee and K. Mondal, Amorphous/Nanocrystalline Composite Coatings Using Blast Furnace Pig Iron Composition by Atmospheric Plasma Spray and Their Electrochemical Response, *J. Therm. Spray Technol.*, 2020, **29**(4), p 843-856. https://doi.org/10.1007/s11666-020-00995-x

13. G.Y. Koga, A.M. Jorge Junior, V. Roche, R.P. Nogueira, R. Schulz, S. Savoie, A.K. Melle, C. Loable, C. Bolfarini, C.S. Kiminami and W.J. Botta, Production and Corrosion Resistance of Thermally Sprayed Fe-Based Amorphous Coatings from Mechanically Milled Feedstock Powders, *Metall. Mater. Trans. A Phys. Metall. Mater. Sci.*, 2018, **49**(10), p 4860-4870. https://doi.org/10.1007/s11661-018-4785-y

14. M. Cherigui, H.I. Feraoun, N.E. Feninehe, H. Aourag and C. Coddet, Structure of Amorphous Iron-Based Coatings Processed by HVOF and APS Thermally Spraying, *Mater. Chem. Phys.*, 2004, **85**(1), p 113-119.

15. J. Cheng, S. Zhao, D. Liu, Y. Feng and X. Liang, Microstructure and Fracture Toughness of the FePSiB-Based Amorphous/Nanocrystalline Coatings, *Mater. Sci. Eng. A*, 2017, **696**(8), p 341-347. https://doi.org/10.1016/j.msea.2017.04.082

16. H. Zhang, Y. Xie, L. Huang, S. Huang, X. Zheng and G. Chen, Effect of Feedstock Particle Sizes on Wear Resistance of Plasma Sprayed Fe-Based Amorphous Coatings, *Surf. Coatings Technol.*, 2014, **258**, p 495-502. https://doi.org/10.1016/j.surfcoat.2014.08.050

17. A. Kumar, S.K. Nayak, A. Banerjee and T. Laha, Multi-Scale Indentation Creep Behavior in Fe-Based Amorphous/Nanocrystalline Coating at Room Temperature, *Mater. Lett.*, 2021, **283**, p 128768.

18. Y. Yang, C. Zhang, Y. Peng, Y. Yu and L. Liu, Effects of Crystallization on the Corrosion Resistance of Fe-Based Amorphous Coatings, *Corros. Sci.*, 2012, **59**, p 10-19.

19. G.Y. Koga, R.P. Nogueira, V. Roche, A.R. Yavari, A.K. Melle, J. Gallego, C. Bolfarini, C.S. Kiminami and W.J. Botta, Corrosion Properties of Fe-Cr-Nb-B Amorphous Alloys and Coatings, *Surf. Coat. Technol.*, 2014, **254**, p 238-243.

20. D. Li, X. Chen, X. Hui, J. Wang, P. Jin and H. Li, Effect of Amorphicity of HVOF Sprayed Fe-Based Coatings on Their Corrosion Performances and Contacting Osteoblast Behavior, *Surf. Coat. Technol.*, 2017, **310**, p 207-213. https://doi.org/10.1016/j.surfcoat.2016.12.092

21. S.K. Nayak, A. Kumar, K. Sarkar, A. Banerjee and T. Laha, Mechanistic Insight into the Role of Amorphicity and Porosity on Determining the Corrosion Mitigation Behavior of Fe-Based Amorphous/Nanocrystalline Coating, *J. Alloys Compd.*, 2020, **849**, p 156624. https://doi.org/10.1016/j.jallcom.2020.156624

22. S.D. Zhang, W.L. Zhang, S.G. Wang, X.J. Gu and J.Q. Wang, Characterisation of Three-Dimensional Porosity in an Fe-Based Amorphous Coating and Its Correlation with Corrosion Behaviour, *Corros. Sci.*, 2015, **93**, p 211-221.

23. S.D. Zhang, J. Wu, W.B. Qi and J.Q. Wang, Effect of Porosity Defects on the Long-Term Corrosion Behaviour of Fe-Based Amorphous Alloy Coated Mild Steel, *Corros. Sci.*, 2016, **110**, p 57-70.

24. C. Zhang, Z. Chu, F. Wei, W. Qin, Y. Yang, Y. Dong, D. Huang and L. Wang, Optimizing Process and the Properties of the Sprayed Fe-Based Metallic Glassy Coating by Plasma Spraying, *Surf. Coatings Technol.*, 2017, **319**, p 1-5. https://doi.org/10.1016/j.surfcoat.2017.03.063

25. L. Qiao, Y. Wu, S. Hong, J. Cheng and Z. Wei, Influence of the High-Velocity Oxygen-Fuel Spray Parameters on the Porosity and Corrosion Resistance of Iron-Based Amorphous Coatings, *Surf. Coat. Technol.*, 2019, **366**(March), p 296-302. https://doi.org/10.1016/j.surfcoat.2019.03.046

26. A. Kumar, S.K. Nayak, P. Bijalwan, M. Dutta, A. Banerjee and T. Laha, Optimization of Mechanical and Corrosion Properties of Plasma Sprayed Low-Chromium Containing Fe-Based Amorphous/Nanocrystalline Composite Coating, *Surf. Coat. Technol.*, 2019, **370**(May), p 255-268. https://doi.org/10.1016/j.surfcoat.2019.05.010

27. C. Suryanarayana and A. Inoue, Iron-Based Bulk Metallic Glasses, *Int. Mater. Rev.*, 2013, **58**(3), p 131-166.

28. H.X. Li, Z.C. Lu, S.L. Wang, Y. Wu and Z.P. Lu, Fe-Based Bulk Metallic Glasses: Glass Formation, Fabrication, Properties and Applications, *Prog. Mater. Sci.*, 2019, **103**(December 2018), p 235-318.

29. S.K. Nayak, A. Kumar, K. Sarkar, A. Pathak, A. Banerjee and T. Laha, A Study on the Corrosion Inhibition of Fe-Based Amorphous/Nanocrystalline Coating Synthesized by High-Velocity Oxy-Fuel Spraying in an Extreme Environment, *J. Therm. Spray Technol.*, 2019, **28**(7), p 1433-1447. https://doi.org/10.1007/s11666-019-00907-8

30. A. Kumar, S.K. Nayak, K. Sarkar, A. Banerjee, K. Mondal and T. Laha, Investigation of Nano- and Micro-Scale Structural Evolution and Resulting Corrosion Resistance in Plasma Sprayed Fe-Based (Fe-Cr-B-C-P) Amorphous Coatings, *Surf. Coatings Technol.*, 2020, **397**(June), p 126058. https://doi.org/10.1016/j.surfcoat.2020.126058

31. L. Zhao and E. Lugscheider, Influence of the Spraying Processes on the Properties of 316L Stainless Steel Coatings, *Surf. Coat. Technol.*, 2003, **162**(1), p 6-10.

32. C. Chattopadhyay, K.S.N.S. Idury, J. Bhatt, K. Mondal and B.S. Murty, Critical Evaluation of Glass Forming Ability Criteria, *Mater. Sci. Technol.*, 2016, **32**(4), p 380-400.

33. B. Ramakrishna Rao, M. Srinivas, A.K. Shah, A.S. Gandhi and B.S. Murty, A New Thermodynamic Parameter to Predict Glass Forming Ability in Iron Based Multi-Component Systems Containing Zirconium, *Intermetallics*, 2013, **35**, p 73-81. https://doi.org/10.1016/j.intermet.2012.11.020

34. R.S. Maurya, A. Sahu and T. Laha, Quantitative Phase Analysis in $Al_{86}Ni_8Y_6$ Bulk Glassy Alloy Synthesized by Consolidating Mechanically Alloyed Amorphous Powder via Spark Plasma Sintering, *Mater. Des.*, 2016, **93**, p 96-103. https://doi.org/10.1016/j.matdes.2015.12.129

35. Y. Wang, S.L. Jiang, Y.G. Zheng, W. Ke, W.H. Sun, X.C. Chang, W.L. Hou and J.Q. Wang, Effect of Processing Parameters on the Microstructures and Corrosion Behaviour of High-Velocity Oxy-Fuel (HVOF) Sprayed Fe-Based Amorphous Metallic Coatings, *Mater. Corros.*, 2013, **64**(9), p 801-810.

36. C. Zhang, R.Q. Guo, Y. Yang, Y. Wu and L. Liu, Influence of the Size of Spraying Powders on the Microstructure and Corrosion Resistance of Fe-Based Amorphous Coating, *Electrochim. Acta*, 2011, **56**(18), p 6380-6388.

37. A. Loganathan, A. Sahu, C. Rudolf, C. Zhang, S. Rengifo, T. Laha, B. Boesl and A. Agarwal, Multi-Scale Tribological and Nanomechanical Behavior of Cold Sprayed Ti_2AlC MAX Phase

Coating, *Surf. Coat. Technol.*, 2018, **334**(November 2017), p 384-393. https://doi.org/10.1016/j.surfcoat.2017.11.067

38. K. Balani, S.P. Harimkar, A. Keshri, Y. Chen, N.B. Dahotre and A. Agarwal, Multiscale Wear of Plasma-Sprayed Carbon-Nanotube-Reinforced Aluminum Oxide Nanocomposite Coating, *Acta Mater.*, 2008, **56**(20), p 5984-5994. https://doi.org/10.1016/j.actamat.2008.08.020

39. H.M. Ha, J.R. Miller and J.H. Payer, Devitrification of Fe-Based Amorphous Metal SAM 1651 and the Effect of Heat-Treatment on Corrosion Behavior, *J. Electrochem. Soc.*, 2009, **156**(8), p C246.

40. Y. Wang, Z.Z. Xing, Q. Luo, A. Rahman, J. Jiao, S.J. Qu, Y.G. Zheng and J. Shen, Corrosion and Erosion-Corrosion Behaviour of Activated Combustion High-Velocity Air Fuel Sprayed Fe-Based Amorphous Coatings in Chloride-Containing Solutions, *Corros. Sci.*, 2015, **98**, p 339-353.

41. Z. Gan, C. Zhang, Z.R. Zhang, Z.J. Chen and L. Liu, Crystallization-Dependent Transition of Corrosion Resistance of an Fe-Based Bulk Metallic Glass Under Hydrostatic Pressures, *Corros. Sci.*, 2021, **179**(April 2020), p 109098. https://doi.org/10.1016/j.corsci.2020.109098

42. M. Wang, Z. Zhou, Q. Wang, Z. Wang, X. Zhang and Y. Liu, Role of Passive Film in Dominating the Electrochemical Corrosion Behavior of FeCrMoCBY Amorphous Coating, *J. Alloys Compd.*, 2019, **811**, p 151962. https://doi.org/10.1016/j.jallcom.2019.151962

43. M. Isakhani-Zakaria, S.R. Allahkaram and H.A. Ramezani-Varzaneh, Evaluation of Corrosion Behaviour of Pb-Co$_3$O$_4$ Electrodeposited Coating Using EIS Method, *Corros. Sci.*, 2019, **157**(September 2018), p 472-480. https://doi.org/10.1016/j.corsci.2019.06.023

44. S.L. Wu, Z.D. Cui, G.X. Zhao, M.L. Yan, S.L. Zhu and X.J. Yang, EIS Study of the Surface Film on the Surface of Carbon Steel from Supercritical Carbon Dioxide Corrosion, *Appl. Surf. Sci.*, 2004, **228**(1-4), p 17-25.

45. M. Wang, Z. Zhou, Q. Wang, L. Wu, Z. Wang and X. Zhang, Long Term Semiconducting and Passive Film Properties of a Novel Dense FeCrMoCBY Amorphous Coating by Atmospheric Plasma Spraying, *Appl. Surf. Sci.*, 2019, **495**(July), p 143600. https://doi.org/10.1016/j.apsusc.2019.143600

46. C. Liu, Q. Bi, A. Leyland and A. Matthews, An Electrochemical Impedance Spectroscopy Study of the Corrosion Behavior of PVD Coated Steels in 0.5 N NaCl Aqueous Solution: Part II. EIS Interpretation of Corrossion Behaviour, *Corros. Sci.*, 2003, **45**(6), p 1257-1273.

47. D. de la Fuente, J. Alcántara, B. Chico, I. Díaz, J.A. Jiménez and M. Morcillo, Characterisation of Rust Surfaces Formed on Mild Steel Exposed to Marine Atmospheres Using XRD and SEM/Micro-Raman Techniques, *Corros. Sci.*, 2016, **110**, p 253-264. https://doi.org/10.1016/j.corsci.2016.04.034

48. K.F. McCarty and D.R. Boehme, A Raman Study of the Systems Fe$_{3-x}$Cr$_x$O$_4$ and Fe$_{2-x}$Cr$_x$O$_3$, *J. Solid State Chem.*, 1989, **79**(1), p 19-27.

49. J.E. Maslar, W.S. Hurst, W.J. Bowers, J.H. Hendricks, M.I. Aquino and I. Levin, In Situ Raman Spectroscopic Investigation of Chromium Surfaces under Hydrothermal Conditions, *Appl. Surf. Sci.*, 2001, **180**(1-2), p 102-118.

Publisher's Note Springer Nature remains neutral with regard to jurisdictional claims in published maps and institutional affiliations.